Localized slip and distributed deformation in oblique settings: the example of the Denali fault system, Alaska

Amaury Vallage, Maud H Devès, Yann Klinger, Geoffrey C.P. King, Natalia A. Ruppert

Geophysical Journal International

Geophys. J. Int. (2014) **197,** 1284–1298
Advance Access publication 2014 April 17

doi: 10.1093/gji/ggu100

Localized slip and distributed deformation in oblique settings: the example of the Denali fault system, Alaska

Amaury Vallage,[1] Maud H. Devès,[1] Yann Klinger,[1] Geoffrey C. P. King[1] and Natalia A. Ruppert[2]

[1] *Tectonique et Mécanique de la Lithosphère, Institut de Physique du Globe de Paris, Sorbonne Paris Cité, Univ Paris Diderot, UMR* 7154 *CNRS, F-*75005 *Paris, France. E-mail: vallage@ipgp.fr*
[2] *Alaska Earthquake Information Center, Geophysical Institute, University of Alaska, Fairbanks, Fairbanks, AK* 99775-7320*, USA*

Accepted 2014 March 14. Received 2014 March 12; in original form 2013 July 23

SUMMARY

In most fault systems the direction of the relative plate motion is oblique to the azimuth of the existing faults. Hence, during earthquakes the displacement may be partitioned between several faults that accommodate different components of the total motion. Here, we quantify the effect of the obliquity of the fault system relatively to the plate-motion direction on the distribution of the deformation in the fault system, during distinct periods of the seismic cycle.

The 2002 November, M_w 7.9, Denali strike-slip earthquake ruptured 341 km of the Denali fault. The azimuth of the fault varies by more than 50° over the total rupture length, making the Denali fault an ideal system to test the effect of obliquity. From west to east, thrust dominates the first part of the rupture while strike-slip dominates the central and eastern sections. Using a kinematic model that considers the obliquity of the plate-motion direction relative to the local fault azimuth, we explored how much of the far-field tectonic loading is accommodated on the main strike-slip fault during the earthquake, and how much is accommodated by distributed deformation off the main fault, on secondary structures. Using a dataset of 735 focal mechanisms, we represent the deformation using strain rosettes and we compare seismological data with model results using the areal strain. Then we developed the parameter *Ca*, the coefficient of accommodation, which allows a direct quantification of the efficiency of a fault to accommodate oblique motion.

Using these indicators, we show that in oblique setting, such as in the Denali case, the aftershocks and the background seismicity are organized to accommodate a significant part of the deformation that is not taken on the Denali strike-slip fault during the main earthquakes. The westward increase of the obliquity actually increases the amount of such deformation accommodated through distributed thrust faults, leading to the westward widening of the Alaska Range, located north of the Denali fault.

Therefore, the strain partitioning between localized slip on pre-established major faults and distributed deformation accommodated through aftershocks and background seismicity on smaller faults (highlighted here by the longer-term topography) seems to be needed during the seismic cycle to accommodate the boundary conditions in such oblique settings.

Key words: Seismic cycle; Continental tectonics: compressional; Continental tectonics: strike-slip and transform; Dynamics and mechanics of faulting; Dynamics: seismotectonics; Mechanics, theory, and modelling.

1 INTRODUCTION

Over geological time, boundary conditions imposed by plate tectonics change. Such changes involve modifications in local plate configuration, hence the boundary conditions experienced by existing structures. The geometry of the tectonic structures however, cannot change as rapidly. Eventually, in many cases, faults are not perfectly oriented to accommodate the total displacement required by the new boundary conditions. Oblique motion relative to the orientation of a specific fault system has been observed in numerous contexts (Fitch 1972; Beck 1991; McCaffrey 1992; Platt 1993; Yu *et al.* 1993; McCaffrey *et al.* 2000; Sieh & Natawidjaja 2000;

Xu *et al.* 2009), including the effect of slip-partitioning, which is often associated with obliquity (Armijo *et al.* 1986; Bowman *et al.* 2003; King *et al.* 2005). The quantification of the effect of the obliquity on the efficiency of a fault system to accommodate boundary conditions, however, has received little attention due to the lack of pertinent data. Here, we take advantage of the 2002 Denali earthquake sequence, which includes a large foreshock, a main shock and a well-documented sequence of aftershocks to quantify the distribution of the deformation on the main fault and on the secondary faults, and to study what part of the deformation is specifically accommodated by each fault.

The Denali Earthquake ruptured the Denali fault system (DFS) in Alaska on 2002 November 3 (Eberhart-Phillips *et al.* 2003). This region accommodates the relative displacement between the North American Plate and the Pacific Plate (Fig. 1, St. Amand 1957). Because of the up-side down L shape of the Northern American Plate, the motion between the Pacific Plate and the Northern American Plate is accommodated to the North by the Aleutian subduction zone, and to the east by the Queen Charlotte strike-slip fault. In the corner, at the junction between these two major tectonic systems, the Alaskan continental lithosphere undergoes substantial deformation accommodated by a limited number of faults bounding microplates. Both GPS and geological studies addressing deformation of this area show that these microplates behave rigidly at least at the timescale of Quaternary deformation (Fitzgerald *et al.* 1993; Freymueller *et al.* 2008). One of the most recently activated continental fault system is the Denali fault system (DFS), formed mainly by two subvertical strike-slip faults, the Denali fault and the Totschunda fault. The DFS is around 700 km long and, from east to west, the DFS strike varies by more than 50° (Fig. 1).

Several kinematic models have considered this geometry to accommodate a counter-clockwise rotation of the Wrangell block (around a close Euler pole located at 59.63°N and 147.38°N) with respect to the stable North American block, and a constant velocity along the DFS (Lahr & Plafker 1980; Fletcher 2002; Bufe 2006; Freed *et al.* 2006; Freymueller *et al.* 2008). However, measurements of slip-rate averaged over the Holocene show that the slip-rate along the DFS is decreasing westward along the DFS, suggesting instead that the Wrangell block is moving northwestward relative to the stable North America (Matmon *et al.* 2006; Mériaux *et al.* 2009). This later interpretation would correspond to a much more distant Euler pole.

The direct consequence of considering the Wrangell block to move northward relative to stable North America, instead of rotating counter-clockwise around a nearby Euler pole, is that obliquity of the DFS relative to the plate-motion direction (i.e. the angle between the DFS and the plate-motion) increases westward along the DFS. This, in turn, implies that the strike-slip faults forming the DFS become less and less well oriented to accommodate the plate motion. In this paper, we explore each tectonic models to examine the relation between the coseismic motion on the DFS, the off-fault deformation associated with the aftershock sequence, and the deformation that occurs at geological timescale.

At the earthquake timescale, the coseismic deformation has been characterized based on focal mechanisms, geodetic measurements and field measurements (Eberhart-Phillips *et al.* 2003; Hreinsdóttir

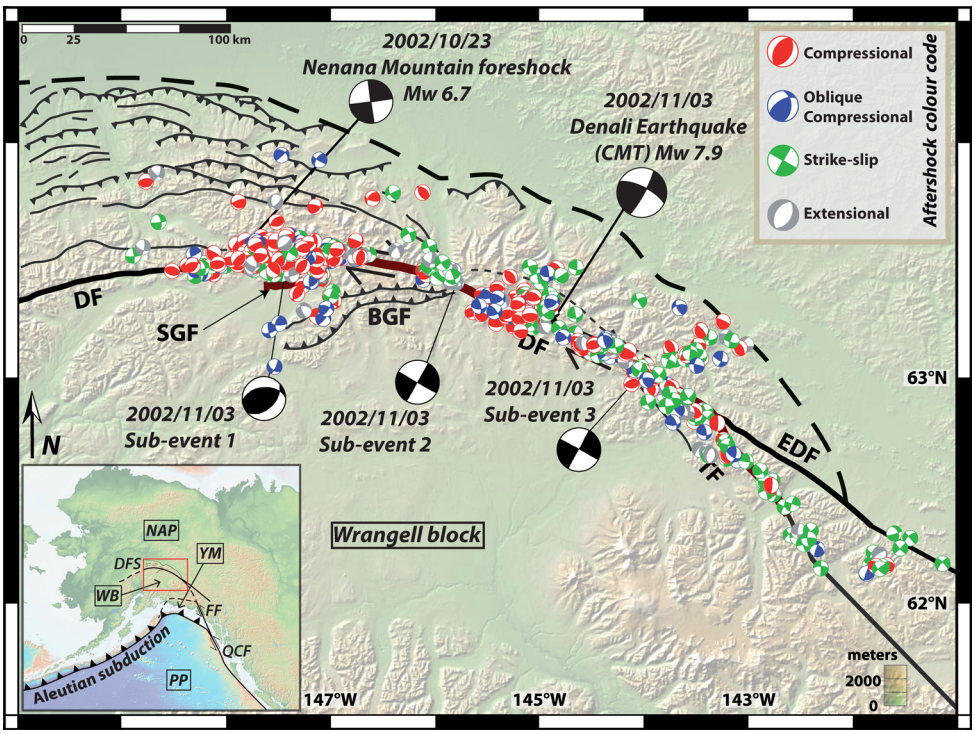

Figure 1. Map of the Denali fault system (DFS), SGF: Susitna Glacier Fault; DF: Denali fault; TF: Totschunda Fault; EDF: eastern Denali fault; BGF: Broxson Gulch Fault; modified from Mériaux *et al.* (2009), Wright *et al.* (2003) and digital data from Haeussler *et al.* (2009) with the focal mechanisms of Nenana mountain precursor and the three subevents of the 2002 earthquake. Other major features are FF: Fairweather Fault; QCF Queen Charlotte Fault and PP: Pacific Plate; YM: Yakutat Microplate; WB: Wrangell Block; NAP: North American Plate. The Mt McKinley is located east of the western edge of the figure, south of DF. The ruptures are shown in thick brown lines. Aftershocks focal mechanisms in red if compressive, in green if strike-slip, in blue if oblique compressive (strike-slip + compression) and in grey if extensive or oblique extensive (strike-slip + extension). The black dashed line north of the fault emphasizes the fact that the zone of thrusting widens westward.

et al. 2003, 2006; Wright *et al.* 2003, 2004; Crone *et al.* 2004; Frankel 2004; Haeussler *et al.* 2004; Elliott *et al.* 2007; Schwartz *et al.* 2012). The Denali earthquake started as a thrust on the Susitna Glacier Fault before propagating eastward on the Denali strike-slip fault and, eventually, branching on the Totschunda Fault (Fig. 1). This earthquake has been accommodating mostly strike-slip motion. Interestingly, numerous aftershocks have been recorded that display a variety of focal mechanisms departing from only pure strike-slip, with a significant component of thrust (Ratchkovski 2003; Ratchkovski *et al.* 2003; Wesson & Boyd 2007). Different behaviours between the main shock and the aftershock sequence have been observed already for earlier earthquakes occurring in oblique tectonic settings, such as for the M_w 7.1 Loma Prieta earthquake, in 1989 (Zoback & Beroza 1993; Kilb *et al.* 1997), or for the more recent M_w 7.9 Wenchuan earthquake, 2008, (Yu *et al.* 2010) which were characterized by a mixture of compression and strike-slip. The Haiti earthquake (2010, M_w 7), which main shock was oblique with a major component of strike-slip and a small reverse component, was mostly followed by compressive aftershocks as well (Nettles & Hjörleifsdóttir 2010). Indeed, it appears fairly common that major earthquakes occurring in oblique settings are associated with particularly complex aftershock patterns.

In the following, we explore the distribution of the deformation between the main fault and the secondary structures due to the obliquity of the DFS relatively to the plate motion. First, we use the strain rosettes to represent the horizontal deformation associated with the earthquakes (Amelung & King 1997b) and we quantify the horizontal deformation using the areal strain. We develop a kinematic model to reproduce the coseismic strain rosettes and the corresponding values of areal strain. We derive from this model a numerical indicator *Ca*, the coefficient of accommodation, which characterizes the efficiency of the fault to accommodate the motion, depending on the obliquity of the fault with respect to the large-scale plate motion. This approach is then used to quantify the amount and style of deformation that is taken up by localized slip on the Denali fault during a large earthquake versus the part of distributed deformation that is taken up by the aftershocks. Finally, we discuss implications of our results on the longer-term deformation pattern.

2 METHODS

2.1 Strain rosette and style of deformation

To visualize the horizontal component of the deformation on a fault we use the strain rosette representation developed by Amelung & King (1997b). For a single earthquake, this representation is similar to a classic focal mechanism. However, unlike focal mechanisms, the strain rosette can also be used to represent deformation inferred from an ascribed fault geometry and boundary conditions or, as detailed in the next section, to look at the deformation due to a group of earthquakes. The strain rosette is a powerful tool that allows for quantitative comparison of deformation style, even if the deformation pattern has been estimated from different sources (one earthquake, sum of several events, output of direct model). The strain rosettes are obtained by plotting the radial component of the strain tensor as a function of the azimuth. The strain tensor can be derived from the earthquake focal mechanism by projecting the normalized displacement recorded on the fault onto the horizontal plane (see methods in Appendix A). Fig. 2 gives examples of strain rosettes associated with classical focal mechanisms. Compressional lobes are shown in white and extensional lobes in black.

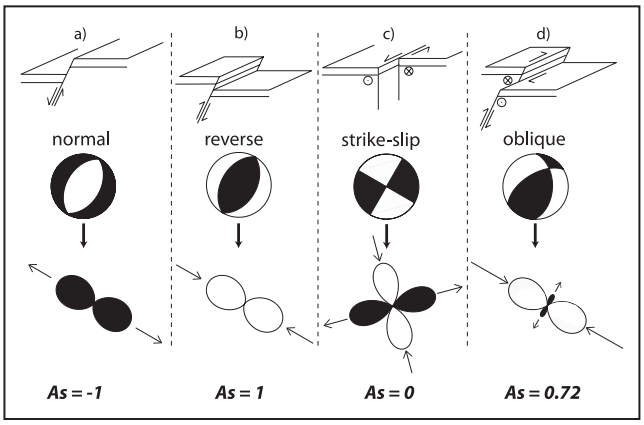

Figure 2. Focal mechanisms and strain rosettes associated with the three conventional types of earthquakes plus an oblique one. (a) The strain rosette resulting from a normal slip event shows two black lobes oriented following the direction of maximum extension. The fault plane can be drawn from the lobes orientation. It lies perpendicularly to the preferential direction of the lobes. (b) The strain rosette resulting from a reverse slip event shows two white lobes oriented following the direction of maximum compression. (c) The strain rosette resulting from a strike-slip event shows four lobes of equal dimensions, the white ones following the direction of maximum compression and the black ones following the direction of maximum extension. (d) The strain rosette resulting from an oblique slip event exhibits four lobes of distinct size. Their relative amplitude reflects the relative amplitude of the extensional and the compressional components of the deformation. The areal strain *As* quantifies the difference in length between the white and the black lobes. In the case shown here, the compressional component dominates over the extensional one with an *As* closer to 1 than to 0.

Working with strain instead of stress presents the advantage that no assumptions on the lithospheric rheological parameters are needed (Ben-Zion 2001; Ben-Zion & Zhu 2002). In addition, projecting all the strain tensors associated with specific focal mechanisms in a common reference system allows the direct summation of the deformation associated with the earthquakes considered (Appendix A, Molnar 1983; Amelung & King 1997b; Bailey *et al.* 2009, 2010). Thus, a singular strain rosette can be determined that describes the total deformation resulting from the effect of several earthquakes.

To get further insights into the deformation pattern, we calculate the areal strain (*As*) that corresponds to the relative change of area associated with the deformation (this is obtained from the trace of the diagonalized strain tensor). In a radial representation, the areal strain corresponds to the difference between the length of the compressional lobe and the length of the extensional lobe of the strain rosette:

$$As = \Delta A / A_0 = \varepsilon_{11} + \varepsilon_{22} = A_1 - A_2.$$

With ΔA the variation in area, A_0 the initial area, A_1 the length of the compressional (white) lobe and A_2 the length of the extensional (black) lobe (note that A_2 is positive whereas ε_{22} is negative).

As is normalized to be between –1 and +1. The value –1 corresponds to a purely extensional rosette, the value 0 to a purely strike-slip rosette and the value +1 to a purely compressional rosette. Oblique extensional and oblique compressional behaviours are characterized by intermediate values (Fig. 2). Because the strain rosette remains the same regardless of the selected nodal plane (fault plane or auxiliary plane), *As* allows for comparison of the deformation associated with earthquakes, even if the actual fault plane is unknown.

Whereas strain rosettes give an immediate representation of the style and the orientation of the deformation, *As* provides a direct quantification of the deformation that has been taken up in extension and compression.

2.2 Kinematic approach

A kinematic approach can also be used to describe the deformation in the case of pre-existing fault structures and to design a parameter that quantifies the efficiency of a fault to accommodate an imposed motion.

A displacement corresponding to far-field boundary conditions is applied to a fault with a specified geometry (strike and dip). The far-field boundary conditions are usually related to large-scale plate tectonics. Here, we consider these displacements to be purely horizontal. The plate motion is called U_{pm} and is defined as a unit vector. λ_{pm} is defined by the angle between U_{pm} and the azimuth of the fault; it corresponds to the horizontal obliquity. In three dimensions the obliquity of the system corresponds to the combination of λ_{pm} and of the dip of the fault. We calculate the slip resulting from the imposed boundary conditions by projecting the motion onto the fault plane, following the direction normal to the fault plane (Fig. 3a). This vector is then re-projected onto the horizontal plane, following the normal to the horizontal plane (Fig. 3b). The resulting vector, U_h, would correspond to the horizontal displacement that can be accommodated by the pre-established fault while subjected to the applied motion. In this approach the along-strike component of the displacement accommodated by the fault is always equal to the along-strike component of the applied motion (*X*-axis in Fig. 3). It is the component normal to the fault strike (*Y*-axis in Fig. 3) that varies with the dip of the fault and with λ_{pm}.

The difference in amplitude and orientation between U_{pm} and U_h varies with λ_{pm} and the dip of the fault. The projection of the vector U_h onto the vector U_{pm}, called the coefficient of accommodation (*Ca*; Fig. 3c, Appendix B), allows us to characterize the efficiency of a fault with a specific geometry to accommodate a motion with an imposed direction. The coefficient *Ca* varies from 0 to 1. For a value of 0, the fault cannot accommodate any of the applied horizontal motion. This situation corresponds to a vertical fault perpendicular to the direction of applied motion. For a value of 1, the fault can fully accommodate the applied horizontal motion. This situation corresponds to a fault parallel to the applied motion (or to a horizontal fault). Most fault systems lie somewhere between these two extreme cases.

As detailed before, the strain rosette can be used to represent the strain tensor associated with focal mechanisms. It can also be used to represent the strain tensor derived from the motion estimated on a given fault plane with our kinematic approach.

3 RESULTS

3.1 Deformation associated with Denali and Nenana Mountain earthquakes

The Denali earthquake was preceded 11 d earlier by the Nenana mountain foreshock (2002 October 23, M_w 6.7, Eberhart-Phillips *et al.* 2003; Wright *et al.* 2003). The foreshock was located along the western part of the Denali fault, less than 25 km away from the epicentre of the Denali earthquake. The strain rosette corresponding to the Nenana earthquake has been derived from the main shock focal mechanism (Fig. 4a). It shows a rosette corresponding to a strike-slip focal mechanism, with white compressional lobes and black extensional lobes of comparable size ($As \sim 0$).

The Denali earthquake (2002 November 3, M_w 7.9) ruptured more than 300 km of the DFS. The earthquake started on the Susitna glacier thrust fault, then propagated eastward along the central part of the Denali fault. Eventually, the rupture ended on the Totschunda strike-slip fault, which branches off the Denali fault (Bhat *et al.* 2004; Haeussler *et al.* 2004; Schwartz *et al.* 2012). Based on first-motion analysis and strong-motion waveform inversion, the Denali earthquake seismic source has been described as the succession of three subevents (Eberhart-Phillips *et al.* 2003; Frankel 2004). Using the focal mechanism determined for each of the three subevents, we could derive individual strain rosettes corresponding to each subevent (Fig. 4a).

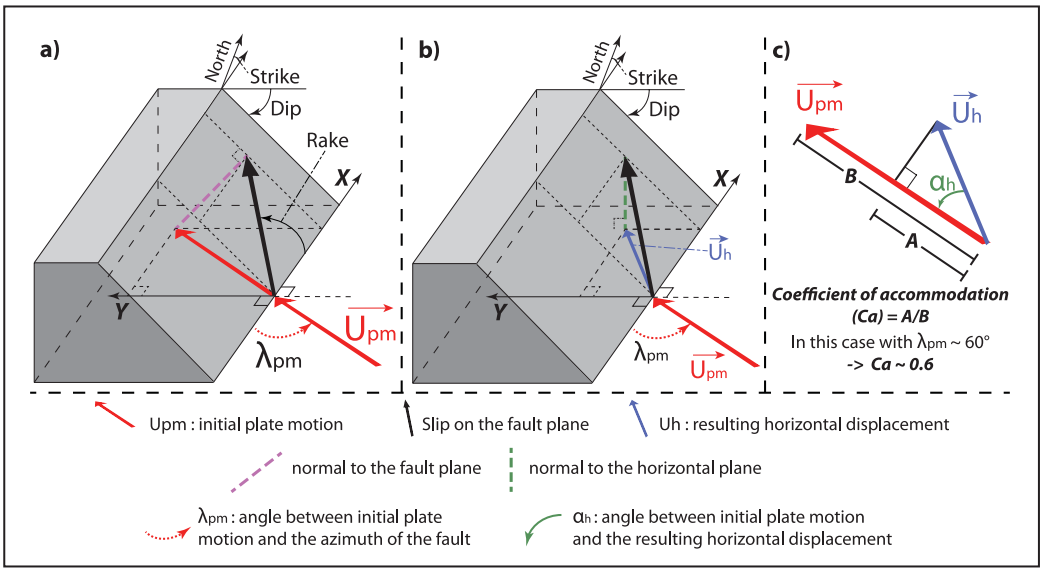

Figure 3. Illustration of the kinematic approach. (a) The plate-motion (red unit vector) is projected onto the fault plane (black arrow) following the normal to the fault (purple dashed line). (b) The slip on the fault (black arrow) is projected back onto the horizontal plane (blue arrow) following the normal to the horizontal plane (green dashed line). (c) The vector corresponding to the horizontal motion accommodated by sliding on the fault is projected onto the vector corresponding to the initial plate motion. The coefficient of accommodation (*Ca*) is the ratio in amplitude between the two vectors.

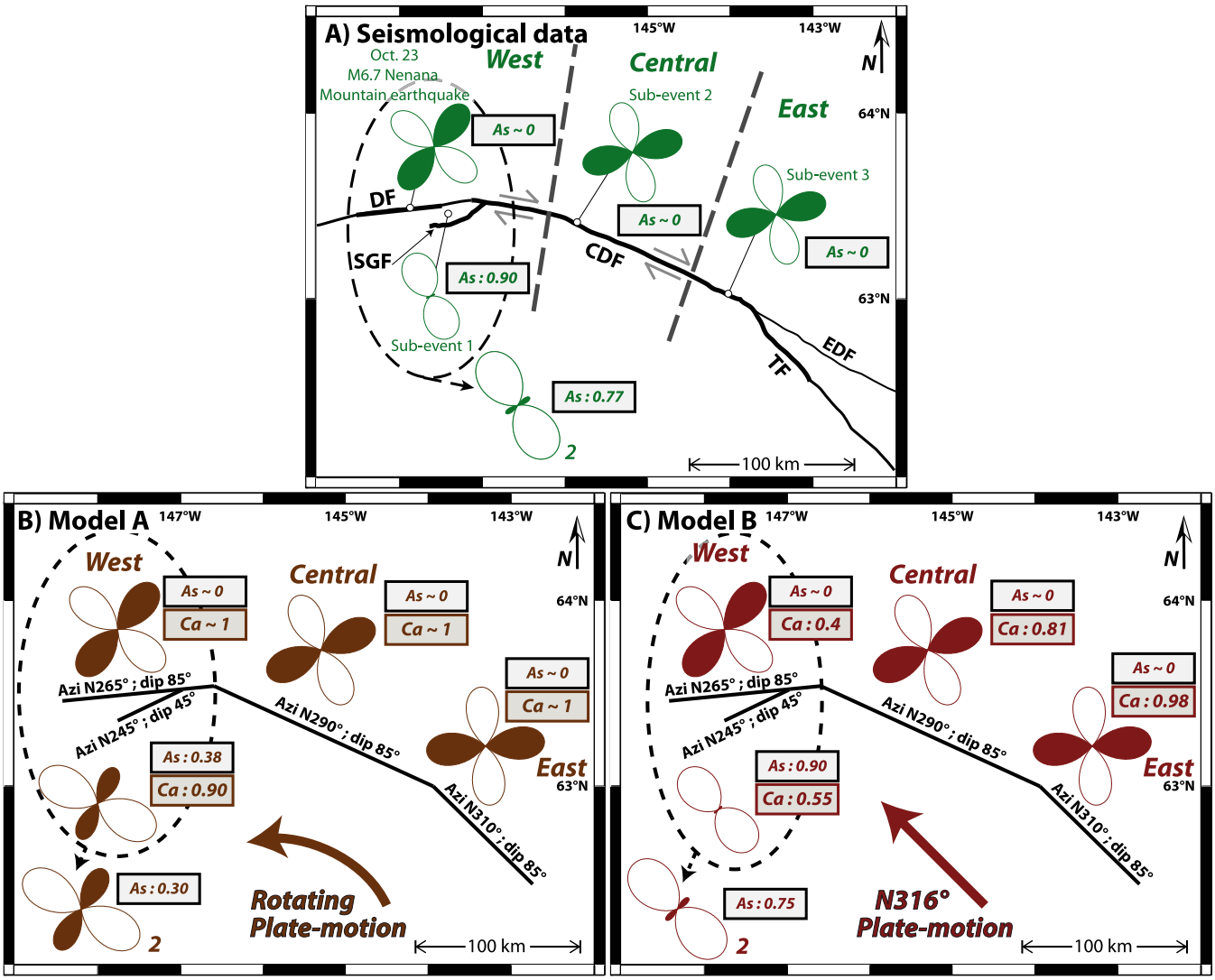

Figure 4. Characteristic of the strain associated with the Nenana mountain foreshock and the Denali earthquake. (a) Strain rosettes and areal strain *As* computed from seismological data of Nenana Mountain earthquake, Denali earthquake subevents and from the Nenana Mountain earthquake summed with the first subevent of Denali earthquake. (b) Predicted strain rosettes using a kinematic model with the Wrangell block rotating along the DFS. The coefficient of accommodation (*Ca*) remains high (close to 1) from east to west. (c) Predicted strain rosettes using a kinematic model where the Wrangell block moves N316° relatively to stable North America. The coefficient of accommodation (*Ca*) decreases from east to west. See discussion on *Ca* in the text.

The first subevent corresponds to the initiation of the Denali rupture on the Susitna Glacier Fault. Both surface ruptures and seismological data suggest that the fault is a thrust fault (Crone *et al.* 2004). The strain rosette we derived from the focal mechanism shows prominent white compressional lobes and small black extensional lobes. The *As* is equal to 0.90, which characterizes the predominance of compression. Strain rosettes for the second and the third subevents, located on the main Denali fault, correspond to strike-slip with white and black lobes of similar size and an *As* close to 0. The rotation of the rosettes from west to east follows the rotation of the azimuth of the main fault.

Using the Nenana earthquake and the subevents of the Denali earthquakes as benchmarks, we have shown that the strain rosette derived from seismological data is an efficient tool to describe the deformation associated to earthquakes. In addition, *As* appears to be effective to characterize the style of deformation into one indicator.

An advantage of using strain rosettes, instead of focal mechanisms, is the possibility to sum the deformation due to several events occurring in a same region, and to represent the resulting deformation with a single rosette. A strain rosette can be calculated that represents all the deformation occurring in the western part of the DFS. This rosette combines the strain contribution of the first Denali subevent and of the foreshock, weighted by their respective seismic moment (Fig. 4a). The resulting strain rosette with an *As* $\sim$ 0.77 shows that total deformation in this part of the DFS is transpressional.

3.2 Kinematic modelling of Denali earthquake

In the previous section, strain rosettes were derived from actual focal mechanisms. Strain rosettes and *As* can also be directly predicted from the deformation pattern associated with ascribed motion on specified fault geometry, using the kinematic model introduced in 2.2. In this section, we compute the rosettes for the fault geometry derived from field observations and different tectonic plate motions proposed in the literature. Then, we compare the predicted rosettes and *As* with the rosettes determined from the seismological data of

the Nenana and the Denali earthquakes. Eventually, the coefficient of accommodation *Ca* is computed for each fault of the model.

The azimuth of each segment of the DFS has been derived from the mapped fault traces published in the literature (Crone *et al.* 2004; Haeussler *et al.* 2004; Haeussler 2009). The dips of the faults are derived from the distribution of the aftershocks (Ratchkovski *et al.* 2004) and from geodetic data inversions (Hreinsdóttir *et al.* 2003, 2006; Wright *et al.* 2003, 2004; Elliott *et al.* 2007). From east to west we can distinguish the Totschunda fault, two Denali segments, central and west, and the Susitna Glacier fault. The Totschunda fault is modelled using a fault segment with an azimuth of N310° and a dip of 85°. The Central part of the Denali fault is modelled using a fault segment with an azimuth of N290° and a dip of 85°. The western part of the Denali fault is modelled using a fault segment with an azimuth of N265° and a dip of 85°. The Susitna Glacier fault is modelled using a fault segment with an azimuth of N245° and a dip of 45°. We have chosen an 85° dip for the subvertical segments to avoid computational singularities. However, varying the dip by ±5° does not change the results significantly.

Although discussing which tectonic model best describes plate motion in Alaska is beyond the scope of this work, our approach allows us to test different models to see how they compare to actual deformation accommodated by earthquakes.

St. Amand (1957) was among the first to notice the circular geometry of the Denali fault. Later, based on small circle hypothesis, Stout & Chase (1980), Fletcher (2002) and Freymueller *et al.* (2008) proposed a rotating block model, with the Wrangell block rotating around an Euler pole located at 59.63°N and 147.38°W. Using this pole (model A, Fig. 4b), we predicted the local orientation of the plate motion acting on the DFS at different locations and derived the associated strain rosette, *As* and *Ca*.

Alternatively, Mériaux *et al.* (2009) proposed that the Euler pole describing the motion between the Wrangell block and North America is located away from the area considered (Fig. 1). The Mériaux *et al.* (2009) kinematic reconstruction, based on moraines offset by the fault, leads these authors to propose a westward reduction in Quaternary slip rates and that the direction of the Wrangell block motion is N316° relative to stable North America. This direction is used as the far-field tectonic boundary condition in model B (Fig. 4c).

In both models, and for each individual segment, we computed the strain rosette, *As*, and *Ca*, to test the efficiency of each segment to accommodate the applied plate motion, depending on their azimuth and their dip (Figs 4b and c). In both models the strain rosettes modelled for the faults segments of Totschunda and Denali show almost pure strike-slip ($As \sim 0$) in good agreement with the rosettes determined from the focal mechanisms for, respectively, the subevent 2, the subevent 3 and the Nenana Mountain earthquake (Fig. 4a). Interestingly the localized deformation remains strike-slip on these faults in model B (Fig. 4c) whereas the obliquity increases westward. This is mainly due to the fault dip. In both models, the azimuth of each modelled strain rosette varies accordingly with the change in the azimuth of the modelled fault planes.

The strain rosette predicted for the Susitna Glacier fault differs for the two models. In model A, the predicted rosette exhibits a strain pattern close to strike-slip deformation. In model B, the rosette exhibits more compression. This is underlined by $As = 0.38$ in model A, and $As = 0.90$ in model B.

In addition, the modelled strain rosette that corresponds to the sum of the contribution of the Susitna Glacier fault and of the western segment of the Denali fault (weighted with the seismic moment of each event) also differs from one model to another. In model A, $As = 0.38$ characterizes this sum. In model B, the sum results in a more compressional rosette with $As = 0.75$.

Thus, the localized deformation varies a lot depending on the model. Because the fault geometry is the same for the two models, these differences can only be due to the local direction of the plate motion.

The strain rosette derived from seismological data of the first subevent alone (on the Susitna Glacier fault) exhibits a large compressional component with $As = 0.90$ (Fig. 4a). When the first subevent (Susitna Glacier fault) is combined with the Nenana Mountain earthquake (western segment of the Denali fault) the value of $As = 0.77$ (Fig. 4a).

Considering that the type of faulting characterizing the 2002 earthquake is representative of the longer term localized deformation in this fault system and by comparing strain rosettes and *As* derived from seismological data with rosettes and *As* predicted from end-member models A and B, it seems that the kinematic model B better reproduces the deformation accommodated by localized slip on the pre-established fault system. Indeed, the actual deformation pattern requires a plate-motion direction which, if not perfectly constant, should be characterized by a consequent westward increase in obliquity with the fault geometry.

Thus, in the following, we choose to consider only the case of a distant Euler pole, similar to model B, to characterize the boundary conditions imposed on the Wrangell block. Under these conditions, and due to the geometry of the fault system, the pattern of deformation accommodated by localized slip (and the derived strain rosettes and *As*) will remain the same for larger or smaller magnitude events localized on these faults.

Figs 5(a) and (b) show how the style of the deformation varies for a given fault when one varies the dip of the fault and the horizontal obliquity λ_{pm}. The results predicted for the different fault segments included in model B are also shown. We can note that for a large range of λ_{pm}, subvertical faults are only able to accommodate the strike-slip component of the motion (*As* is insensitive to λ_{pm} for dips close to 90°, Fig. 5(a). On the contrary, faults with lower dips can accommodate different proportions of strike-slip and compressional (or extensional) displacements, depending on λ_{pm}. Hence, the Totschunda fault as well as the central and western Denali segments accommodate almost only pure strike-slip motion despite the fact that λ_{pm} varies along strike. With a lower dip, the Susitna fault accommodates a larger component of compression, which is interpreted as the result of larger horizontal obliquity λ_{pm}.

Variations in the value of *Ca* for different fault segments of model B (Fig. 5b) show that whereas the motion remains strike-slip on vertical faults for almost all λ_{pm}, the amount of motion actually accommodated by each fault is not the same for similar ascribed far-field tectonic motion. Vertical faults subjected to large λ_{pm} are not able to fully accommodate the imposed boundary conditions. *Ca* decreases from east to west on the Totschunda and central Denali segments to eventually reach a low value of $Ca = 0.4$ for the western Denali segment. On the contrary, a fault with a lower dip could better accommodate a greater variety of boundary conditions as shown by values of *Ca* on average closer to 1 for the full range of λ_{pm}. Actually, along the western part of the DFS, the value of *Ca* is the smallest where λ_{pm} is the largest. There, $Ca \sim 0.4$, indicates that the western Denali fault accommodates less than half of the tectonic plate motion, while the Sustina thrust fault, almost parallel to the western Denali fault, with $Ca = 0.55$ accommodates a significant part of the deformation. For the Sustina fault, *As* is about 0.9, which is characteristic of a compressional regime. Hence, the western region of the DFS presents evidence of partitioning of the

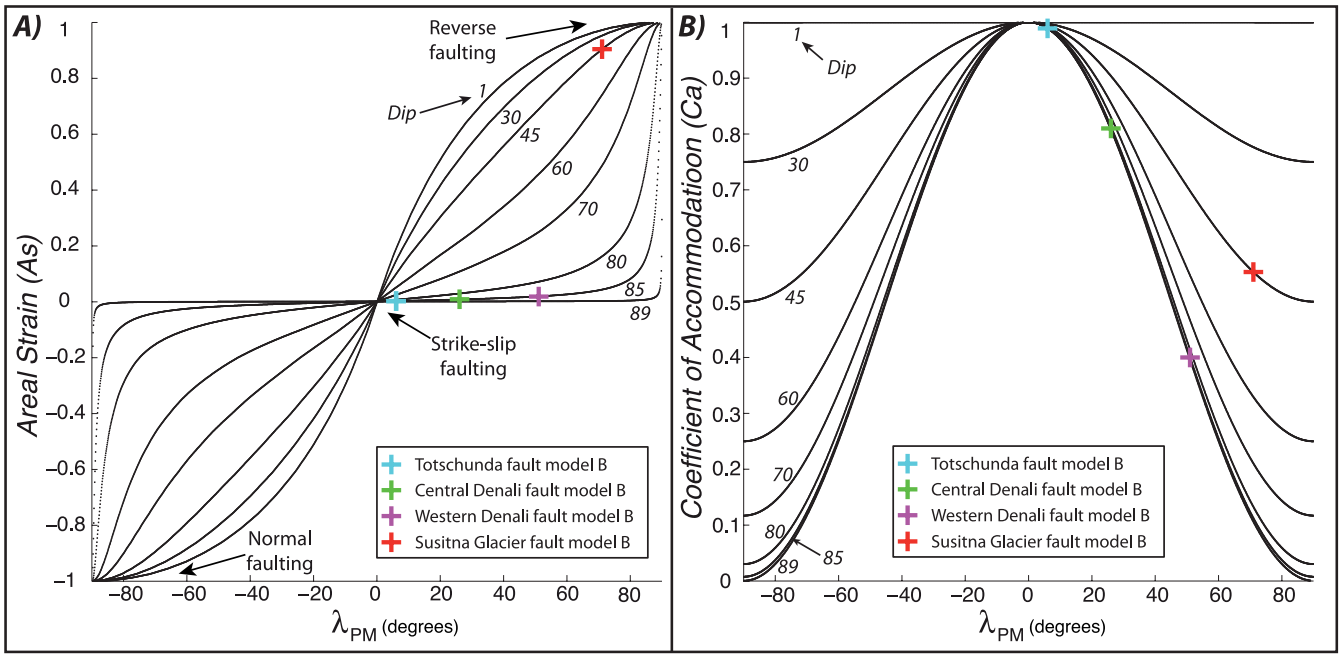

Figure 5. Characterization of the strain accommodated for given fault geometry (dip and obliquity with respect to the applied plate motion). (a) Variation of the areal strain *As* as a function of the fault obliquity and dip. (b) Variation of the coefficient of accommodation *Ca* as a function of the fault obliquity and dip. The points correspond to the faults modelled in Fig. 4(c).

displacement during the Denali earthquake sequence between the strike-slip motion, taken by the western Denali segment, and the compressional motion taken by the Sustina fault (Bowman *et al.* 2003; King *et al.* 2005). Unlike previous earthquakes where slip-partitioning was observed to affect simultaneously the different fault segments accommodating the different components of slip (Klinger *et al.* 2005), during the Denali earthquakes sequence a short time delay was observed between the activation of the different faults accommodating the different part of the motion as the Nenana earthquake (accommodating the strike-slip component in the western part of the sequence) preceded the Denali first subevent (accommodating the thrust component) by 11 d.

3.3 Study of the deformation accommodated by the aftershocks

The computation of *Ca* for the preferred model B (Fig. 4b) shows that the far-field motion is not accommodated in totality by Denali main shock type of earthquake, even when one includes the Nenana foreshock. The strain rosette, because it allows the summation of individual strain contribution for a set of earthquakes, can be used to quantify how much strain is accommodated by the aftershock sequence, and if any specific style of deformation dominates the sequence.

Based on the evolution of the cumulative number of earthquakes for the regional catalogue between 2002 and 2011 as a function of time (Appendix C), we selected 473 events between 2002 November and 2004 December that correspond to the Denali aftershocks sequence. Their magnitudes range between 2.8 and 5.4. The 185 earthquakes occurring between 2005 and 2011 are considered to be representative of the background seismicity (with magnitudes between 2.6 and 4.6), as well as the 71 earthquakes occurring between 1987 and 2002 (with magnitudes between 2.4 and 5.5). They will be treated in a further section.

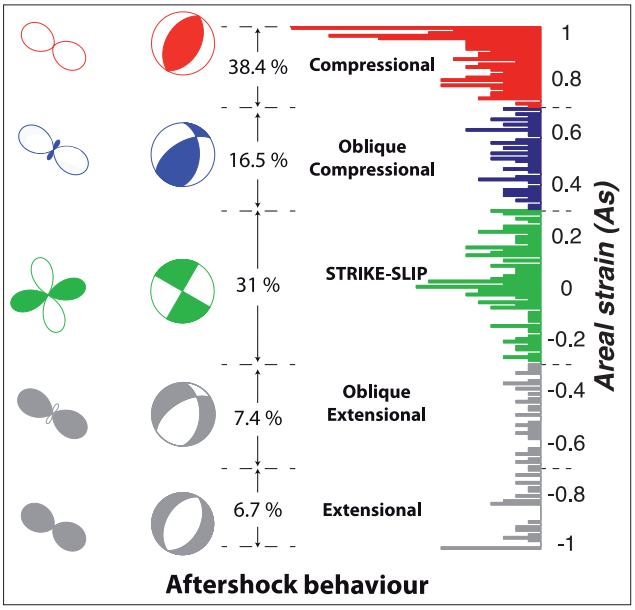

Figure 6. Characterization of the strain accommodated by Denali's aftershocks. Extensional, oblique extensional, strike-slip, oblique compressional and compressional events are shown in different colours, respectively grey, grey, green, blue and red. Percentages express the proportion of aftershocks falling into each class.

A strain rosette and *As* are calculated for each of the 473 aftershock (Fig. 6). Purely compressional mechanisms plot as $As = 1$, purely strike-slip mechanisms as $As = 0$, and purely extensional mechanisms as $As = -1$. Intermediate values of *As* correspond to oblique mechanisms. We arbitrarily choose to split the extensional and the compressional domains at $As = 0.33$ and 0.66, which lead to the following distribution (Table 1):

Table 1. The different domains of areal strain and their interpretation.

$-1 \leq As < -0.7$	Domain of extensional deformation
$-0.7 < As < -0.3$	Domain of oblique extensional deformation
$-0.3 < As < +0.3$	Domain of strike slip deformation
$+0.3 < As < +0.7$	Domain of oblique compressional deformation
$0.7 < As \leq 1$	Domain of compressional deformation

Fig. 6 shows that the aftershocks exhibit many different styles. The domain of compressional deformation accounts for 38.4 per cent of the catalogue ($As > 0.7$, in red). The domain of strike-slip deformation, a deformation similar to the main shock, includes 31 per cent of the aftershocks ($-0.3 < As < +0.3$, in green). Aftershocks falling between these two domains represent 16.5 per cent; of the catalogue and account for oblique compressional deformation ($+0.3 < As < +0.7$, in blue). Aftershocks accounting for oblique extensional and extensional deformation represent only 7.4 and 6.7 per cent, respectively (both in grey, $-0.7 < As < -0.3$ and $As < -0.7$, respectively). Therefore, aftershocks with a component of compression represent more than 50 per cent of the whole aftershock sequence, unlike the main shock and the foreshock, which are dominated by strike-slip.

To visualize the strain accommodated by a group of aftershocks we use a strain rosette approach similar to that developed by Amelung & King (1997b) in California. The strain tensor is derived from the geometric moment, which can be expressed as $\boldsymbol{M}_{ij}$ equivalent to $M.R_{\theta\Phi}$, with M the scalar moment and $R_{\theta\Phi}$ the radial component (Amelung & King 1997b). Classes of magnitudes are defined such as the transition between two successive classes corresponds to a doubling in fault length, which also corresponds to a factor of 8 in scalar moment (Bakun *et al.* 1986; King *et al.* 1994; Amelung & King 1997a,b). Strain rosettes for each class of magnitude are presented in Fig. 7. The strain rosettes exhibit a large similarity in terms of orientation and shape. This similarity allows us to check that strain patterns are independent of earthquake size (self-similarity of the fault system, King 1983) and it suggests that each class is representative of the overall deformation, showing the completeness of the seismic catalogue. Following Amelung & King (1997b), once self-similarity has been verified, one can compute strain rosettes in the area of interest without taking the seismic moment of each event into account (methods in Appendix A). Only the radial component $R_{\theta\Phi}$ is of interest. To check the impact of considering, or not, the seismic moment, both cases will be further represented in the study of aftershocks (Figs 8a and b).

Aftershock strain rosettes (Fig. 7) show a dominant component of compression for all classes of magnitudes, with an As around 0.7–0.8. This component of compression was absent in the main shock sequence. Many aftershocks do not occur on the main fault but rather in the surrounding volume (Liu *et al.* 2003); such distributed seismicity might be responsible for off-fault deformation releasing strain that could not be accommodated by the main shock of the Denali sequence, although required by the oblique boundary conditions (King 1983, 1986; King & Nábělek 1985; Bailey *et al.* 2010; Devès *et al.* 2011).

Aftershocks can be further grouped spatially (east, central and west) to look at the impact of fault geometry in more detail. For each case rosettes including, or not, seismic moment are presented to cross check that if self-similar, removing the scalar moment is a valid working assumption (Figs 8a and b).

We first describe the aftershock strain rosettes obtained without taking the seismic moment into account (Fig. 8a).

The strain rosette for the eastern region corresponds to the deformation accommodated by 74 aftershocks. It shows a combination of strike-slip and compressional strain, with an $As = 0.31$. Although, for an individual earthquake the strike of the corresponding strain rosette should be similar to the azimuth of the fault, for the aftershocks in the eastern region, the average strain rosette strike (the line that can be drawn, passing between white and black lobes, with an angle of N°346) differs from the azimuth of the Totschunda segment (TF, ∼N310°). This difference results from the distribution of the deformation associated with aftershocks, not only occurring on the Totschunda fault but also on smaller faults with different orientations in the surrounding volume.

The strain rosette for the Central region corresponds to the deformation accommodated by 160 aftershocks. The rosette is strike-slip with a large compressional component as indicated by an $As = 0.58$. The average rosette strike (N°317) differs from the azimuth of the central Denali segment (∼N290°). As for the eastern region, this difference seems to be the expression of the distribution of the deformation on and off fault, with a significant scattering of aftershocks epicentres north of the fault.

The strain rosette for the western region corresponds to the deformation accommodated by 205 aftershocks. The rosette is predominantly compressive with an $As = 0.69$. The average strike (N°270) is similar to the strike of the western part of the Denali fault. Interestingly the strain rosette for the western group of aftershocks, by its orientation and by exhibiting a large compressional component, is quite similar to the strain rosette corresponding to the sum of the Nenana earthquake and of the first Denali subevent (Fig. 4). Hence, the two shocks taken together, as well as the aftershock cluster, both reflect the deformation imposed by oblique far-field conditions. Unlike other sections of the rupture, however, the partitioning of the deformation is more pronounced with two distinct fault segments each accommodating specific part of the deformation.

These rosettes obtained without taking the moment into account can then be compared with strain rosettes in which the moment of each earthquake is taken into account (Fig. 8b).

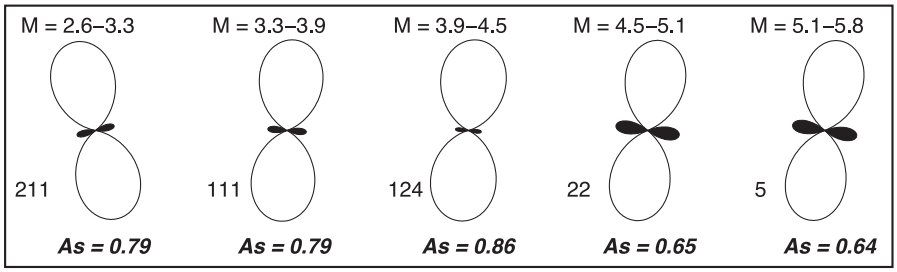

Figure 7. Strain rosettes associated with aftershocks ordered by range of magnitude (M). The number of aftershocks falling into each class of magnitude is indicated on the side of the rosette, as well as the areal strain characterizing them. This representation allows one to test the completeness of the catalogue (Amelung & King 1997a,b).

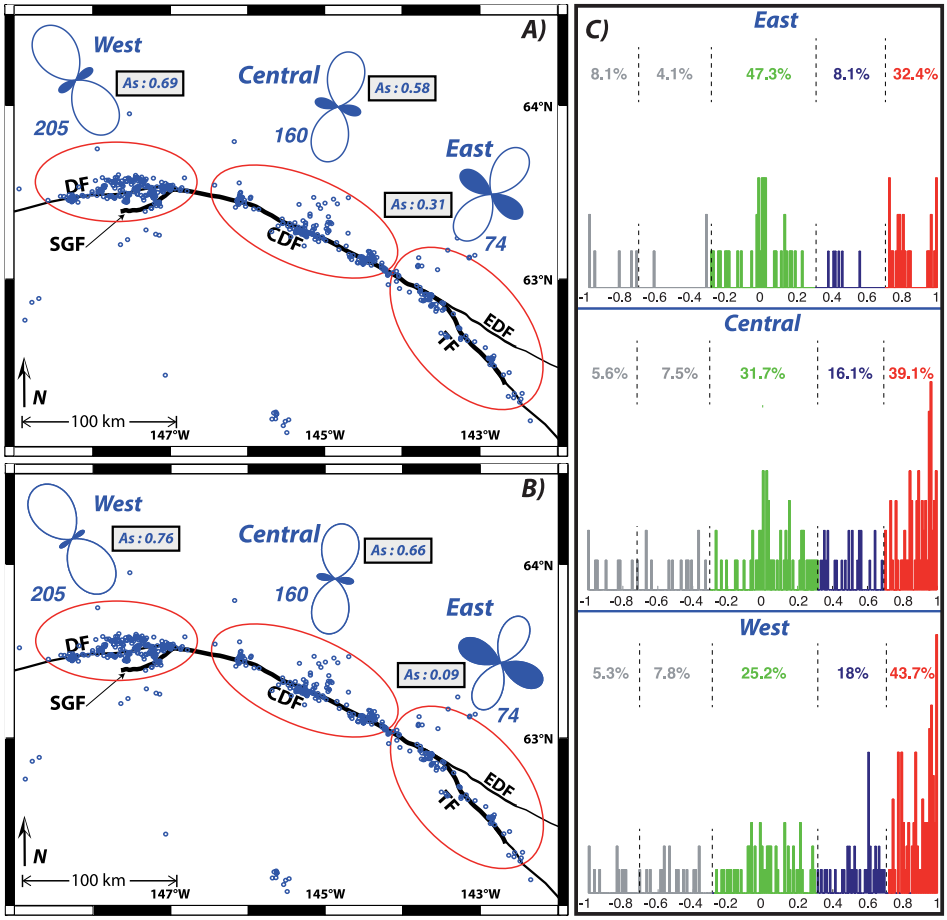

Figure 8. Characterization of the strain associated with aftershocks. (a) The strain rosettes correspond to the strain accommodated by groups of aftershocks. The patches are defined to correspond to the main changes in the fault geometry. The number of events that are summed in each patch is indicated next to each rosette, as well as the areal strain (*As*). The sum is realized without taking into account the seismic moment of each event. (b) Same as (a) but the sum takes into account the seismic moment of each event. (c) Histogram of the Areal Strain (*As*) for each patch of aftershocks (same colour code as in Fig. 6).

The orientation of each rosette does not vary significantly between Figs 8(a) and (b). Furthermore, if each pair of rosettes taken alone can exhibit small variations in terms of shape (and so of *As*), the general pattern of deformation is similar to the one described above when the seismic moment was not taken into account, confirming the self-similarity of the seismic sequence.

Fig. 8(c) shows histograms of *As* for the three regions during the aftershock period, with the same colour code as in Fig. 6. Because each event is represented individually, histograms do not vary whether or not the seismic moment is taken into account. Going from east to west, the proportion of aftershocks accommodating strike-slip (in green) decreases from 47.3 to 25.2 per cent (31.7 per cent for the central region). At the opposite, the proportion of aftershocks accommodating compressional strain (in red) increases from 32.4 per cent in the eastern part (less than the strike-slip proportion in the same area) to 39.1 per cent in the central part, to eventually become the largest part of the aftershocks in the western section with 43.7 per cent. The proportion of aftershocks accommodating oblique compressional strain (in blue) follows the same east to west trend as the purely compressive one. Finally, the proportion of aftershocks accommodating extension remains below 10 per cent everywhere.

This histogram representation confirms that compression and strike-slip aftershocks dominate with a swap of the dominant process when moving from east to west. This swap between strike-slip and compression is consistent with the decrease of *Ca*, predicted from the kinematic model B, as the obliquity between the fault and the plate-motion direction increases westward. Most of the aftershocks actually occur in the area where the obliquity is the largest and thus where *Ca* is the lowest. Aftershocks, which deformation style differs more and more westward from the deformation associated to the main shock sequence, seem therefore organized in this oblique setting to accommodate the missing component of the deformation that is not taken up by the main shock sequence.

3.4 Study of the background seismicity

In the previous section, it has been shown that the aftershocks accommodate a part of oblique far-field conditions that is not accommodated by the Denali earthquake itself and its foreshock. The aftershocks, however, represent a total released moment of 9.2×10^{17} N.m, which remains small compared to the Denali earthquake moment of 6.8×10^{20} N.m (Frankel 2004). Although the seismic catalogue has fewer events, the strain rosette can also be computed for interseismic periods, from 1987 to 2002 (Fig. 9b, 71 events representing a total released moment of 2.2×10^{17} N.m), and after the aftershock period, between 2005 and 2011 (Fig. 9a, 185 events representing a total released moment of 3.8×10^{16} N.m). For the 2005–2011 period, the strain rosettes are similar in orientation and shape to that of the aftershocks (Figs 9a and 8a). We observe a

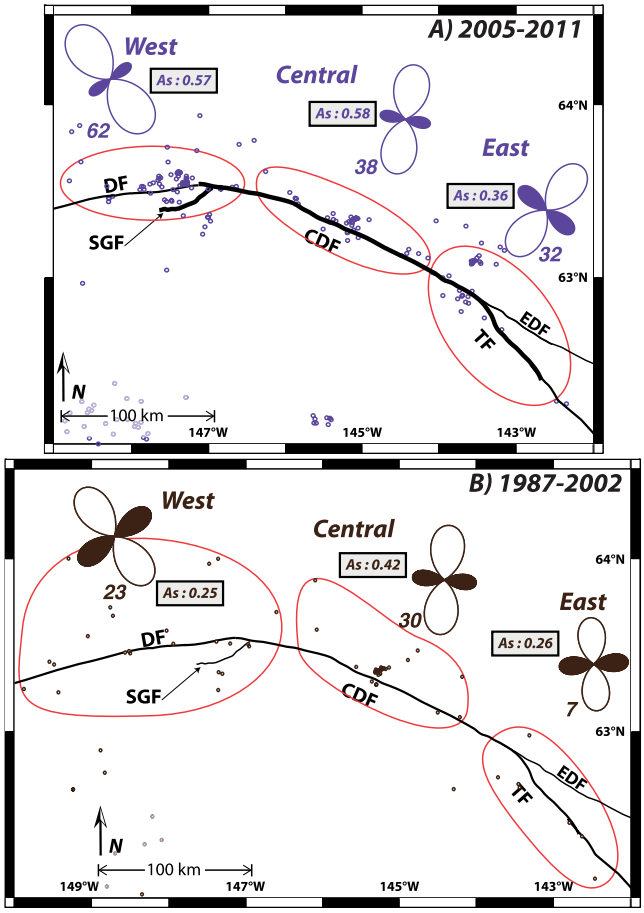

Figure 9. Characterization of the strain accommodated by the background seismicity. (a) The strain rosettes correspond to the strain accommodated by patches of earthquakes during the period 2005–2011. (b) The strain rosettes correspond to the strain accommodated by patches of earthquakes during the period 1987–2002. Due to the very small amount of data each rosette is loosely constrained, these rosettes must be interpreted with caution.

similar increase of the compressional component and variations in orientation from east to west. A very small number of events characterize the period 1987–2002. In consequence, larger grouping areas are required and the resulting rosettes are not as robust as for the other two periods. Adding or removing one or two events with different focal mechanisms can substantially modify the rosettes, for example in the east region, which includes only seven events. It is clear that for this period the assumption of self-similarity of the seismicity does not hold. Despite these loosely constrained rosettes, the pattern of deformation accommodated is generally similar to that of the two other periods, with rotation between rosettes and the presence of compressional deformation. The strain accommodated by the aftershocks is thus comparable to the strain derived from the background seismicity at distinct periods of the seismic cycle. Both are different from the strain accommodated by major earthquakes on the main faults. Hence, the aftershocks and the background seismicity on one side, and the localized slip during major earthquake on the other side, they appear to accommodate complementary components of the deformation, showing an example of slip-partitioning both in space and in time.

The western region is slightly different from the rest of the DFS. That region, where the obliquity is the largest, is characterized by the existence of the Susitna Glacier thrust where the Denali rupture started (Crone *et al.* 2004). One could then hypothesize that in regions where the obliquity is large enough, the fault system will evolve in a way where the oblique slip is accommodated more efficiently by two mature faults, to allow a full slip-partitioning over the longer-term (Bowman *et al.* 2003; King *et al.* 2005). In the case of Alaska, if slip does not occur on the Susitna Glacier fault for each 'Denali like' earthquake, other reverse fault structures might be candidates to be the location of such partitioning (with the Broxson Gulch fault close to the east, or the thrusts near Mt. McKinley to the west; J. Freymueller, personal communication, 2014).

4 EARTHQUAKES AND LONG-TERM DEFORMATION

The deformation accommodated during the Denali earthquake sequence demonstrably varies along strike. A simple kinematic approach, assuming an oblique plate motion vector, shows that the ability of the pre-established faults to accommodate the applied plate motion decreases from east to west. Aftershocks, as well as the diffuse background seismicity, appear to accommodate mostly the compressional component of the deformation, whereas the large earthquakes located on the more mature and vertical faults tend to accommodate rather the strike-slip component. Hence, the westward widening of the topography (Mériaux *et al.* 2009) observed north of the strike-slip fault, which is formed of several active thrusts (Bemis *et al.* 2012), is consistent with a westward increase of the obliquity. Thus, the relationship observed between the deformation localized on the main Denali fault and the deformation distributed on a myriad of secondary faults is probably critical to shape the topography on the timescale of several earthquake cycles (Devès *et al.* 2011).

5 SUMMARY AND DISCUSSION

Purely localized deformation only occurs under very specific boundary conditions (Fig. 5b), while total, or partial, deformation partitioning is commonly observed in oblique tectonic settings. Earthquakes occurring in such oblique tectonic settings, such as the Denali earthquake sequence, are usually associated with a pattern of aftershocks presenting focal mechanisms that can be quite different from that of the main shock. Although a full discussion of the tectonic context of the DFS is beyond the scope of this work, a simple kinematic model shows that a model with a constant direction of motion of the Wrangell block relative to North America fits the deformation pattern well. As the azimuth of the DFS changes by about 50° along the length of the 2002 Denali rupture, the DFS offers an example where the effect of changing obliquity can be easily tested.

We developed three indicators, the strain rosette, areal strain *As* and the coefficient of accommodation *Ca* to characterize the type of deformation associated to one or several earthquakes, and to quantify the efficiency of a specific fault to accommodate given boundary conditions. These indicators were used to characterize the foreshock–main shock–aftershock sequence of the Denali earthquake.

We show that the strike-slip component of the deformation accommodated on the main faults represents a decreasing part of the total regional boundary conditions when moving from east to west and that at the same time the number of aftershocks, dominated by compressional mechanisms, is increasing. It suggests that aftershocks, as well as background seismicity, are organized in space to complement the deficit of deformation that cannot be accommodated any more on the main subvertical fault as obliquity increases.

Strain rosettes allow actual quantification of strain partitioning at a larger timescale, beyond the occurrence of slip partitioning during a single earthquake. These aftershocks and microseismicity are mostly accommodated by secondary structures with dips that can be far from vertical. Eventually, one could hypothesize that when the obliquity becomes too large, the tectonic system would reorganize itself to promote localization of the deformation along a fault better oriented relatively to the boundary conditions, such as the Sustitna Glacier thrust fault in the case of the DFS.

ACKNOWLEDGEMENTS

We thank R. Dmowska and A.-S. Mériaux for useful discussions. We are grateful to the editor, Y. Ben-Zion, and two anonymous reviewers for their helpful comments. This work has been done in the framework of the ANR GEOSMEC contract ANR-12-BS06–0016. MD acknowledges some support from the European Research Council (ERC Project 269586 DISPERSE). This research was supported in part by the office of Alaska State Seismologist. This is IPGP contribution number 3505.

REFERENCES

Amelung, F. & King, G.C.P., 1997a. Earthquake scaling laws for creeping and non-creeping faults, *Geophys. Res. Lett.,* **24**(5), 507–510.

Amelung, F. & King, G.C.P., 1997b. Large-scale tectonic deformation inferred from small earthquakes, *Nature,* **386,** 702–705.

Armijo, R., Tapponnier, P., Mercier, J.L. & Han, T.L., 1986. Quaternary extension in southern Tibet—field observations and tectonic implications, *J. geophys. Res.,* **91,** 13 803–13 872.

Bailey, I.W., Becker, T.W. & Ben-Zion, Y., 2009. Patterns of co-seismic strain computed from Southern California focal mechanisms, *Geophys. J. Int.,* **177,** 1015–1036.

Bailey, I.W., Ben-Zion, Y., Becker, T.W. & Holschneider, M., 2010. Quantifying focal mechanism heterogeneity for fault zones in Southern and Central California, *Geophys. J. Int.,* **183,** 433–450.

Bakun, W.H., King, G.C.P. & Cockerham, R.S., 1986. Seismic slip, aseismic slip and the mechanics of repeating earthquakes on the Calaveras fault, California, in *Earthquakes Source Mechanics,* AGU Geophysical Monograph 37, pp. 195–207, American Geophysical Union.

Beck, M.E., 1991. Coastwise transport reconsidered: lateral displacements in oblique subduction zones, and tectonic consequences, *Phys. Earth planet. Inter.,* **68,** 1–8.

Bemis, S.P., Carver, G.A. & Koehler, R.D., 2012. The Quaternary thrust system of the northern Alaska Range, *Geosphere,* **8(1)**, 196–205.

Ben-Menahem, A. & Singh, S.J., 1981. *Seismic Waves and Sources,* Springer-Verlag.

Ben-Zion, Y., 2001. A note on quantification of the earthquake source, *Seism. Res. Lett.,* **72,** 151–151.

Ben-Zion, Y. & Zhu, L., 2002, Potency-magnitude scaling relations for southern California earthquakes with 1.0 < Ml < 7.0, *Geophys. J. Int.,* **148,** F1–F5.

Bhat, H.S., Dmowska, R., Rice, J.R. & Kame, N., 2004. Dynamic slip transfer from the Denali to Totschunda Faults, Alaska: testing Theory for fault branching, *Bull. seism. Soc. Am.,* **94**(6B), S202–S213.

Bowman, D., King, G.C.P. & Tapponnier, P., 2003. Slip partitioning by elastoplastic propagation of oblique slip at depth, *Science,* **300,** 1121–1123.

Bufe, C.G., 2006. Coulomb stress transfer and tectonic loading preceding the 2002 Denali fault earthquake, *Bull. seism. Soc. Am.,* **96**(5), 1662–1674.

Crone, A.J., Personius, S.F., Craw, P.A., Haeussler, P.J. & Staft, L.A., 2004. The Susitna Glacier Thrust Fault: characteristics of surface ruptures on the fault that initiated the 2002 Denali Fault earthquake, *Bull. seism. Soc. Am.,* **94**(6B), 5–22.

Devès, M., King, G.C.P., Klinger, Y. & Agnon, A., 2011. Localized and distributed deformation in the lithosphere: modelling the Dead Sea region in 3 dimensions, *Earth. planet. Sci. Lett.,* **308,** 172–184.

Eberhart-Phillips, D. *et al.*, 2003. The 2002 Denali Fault Earthquake, Alaska: a large magnitude, slip-partitioned event, *Science,* **300,** 1113–1118.

Elliott, J.L., Freymueller, J.T. & Rabus, B., 2007. Coseismic deformation of the 2002 Denali fault earthquake: contributions from synthetic aperture radar range offsets, *J. geophys. Res.,* **112,** 1–19.

Fitch, T.J., 1972. Plate convergence, Transcurrent Faults, and internal deformation adjacent to Southeast Asia and the Western Pacific, *J. geophys. Res.,* **77,** 4432–4460.

Fitzgerald, P.G., Stump, E. & Redfield, T.F., 1993. Late Cenozoic uplift of Denali and its relation to relative plate motion and fault morphology, *Science,* **259**(5094), 497–499.

Fletcher, H.J., 2002. Crustal deformation in Alaska measured using the global positioning system, *PhD thesis*, Univ. of Alaska Fairbanks, 135 pp.

Frankel, A., 2004. Rupture process of the M 7.9 Denali Fault, Alaska, Earthquake: subevents, directivity, and scaling of high-frequency ground motions, *Bull. seism. Soc. Am.,* **94**(6B), 234–255.

Freed, A.M., Bürgmann, R., Calais, E., Freymueller, J. & Hreinsdóttir, S., 2006. Implications of deformation following the 2002 Denali, Alaska, earthquake for postseismic relaxation processes and lithospheric rheology, *J. geophys. Res.,* **111**, B01401, doi:10.1029/2005JB003894.

Freymueller, J.T., Woodard, H., Cohen, S.C., Cross, R., Elliott, J., Larsen, C.F., Hreinsdóttir, S. & Zweck, C., 2008. Active deformation processes in Alaska, based on 15 years of GPS measurements, in *Active Tectonics and Seismic Potential of Alaska*, AGU Geophysical Monograph 179, pp. 1–42, American Geophysical Union.

Gilbert, F., 1970. Excitation of the normal modes of the Earth by earthquake sources, *Geophys. J. R. astr. Soc.,* **22,** 223–226.

Haeussler, P.J., 2009. Surface rupture map of the 2002 M7.9 Denali Fault earthquake, Alaska; Digital Data: U.S., *Geological Survey Data Series,* 422 [http://pubs.usgs.gov/ds/422/].

Haeussler, P.J. *et al.*, 2004. Surface rupture and slip distribution of the Denali and Totschunda Faults in the 3 November 2002 M 7.9 Earthquake, Alaska, *Bull. seism. Soc. Am.,* **94**(6B), 23–52.

Hreinsdóttir, S., Freymueller, J.T., Fletcher, H.J., Larsen, C.F. & Bürgmann, R., 2003. Coseismic slip distribution of the 2002 Mw7.9 Denali fault earthquake, Alaska, determined from GPS measurements, *Geophys. Res. Lett.,* **30**(13), 1–4.

Hreinsdóttir, S., Freymueller, J.T., Bürgmann, R. & Mitchell, J., 2006. Coseismic deformation of the 2002 Denali Fault earthquake: insights from GPS measurements, *J. geophys. Res.,* **11,** 1–18.

Kilb, D., Ellis, M., Gomberg, J. & Davis, S., 1997. On the origin of diverse aftershock mechanisms following the 1989 Loma Prieta earthquake, *Geophys. J. Int.,* **128,** 557–570.

King, G.C.P., 1978. Geological faults, fractures, creep and strain, *Phil. Trans. R. Soc. Lond., A.,* **288,** 197–212.

King, G.C.P., 1983. The accommodation of large strains in the upper lithosphere of the Earth and other solids by self-similar fault systems: the geometrical origin of b-value, *Pure appl. Geophys.,* **121,** 761–815.

King, G.C.P. & Nábělek, J., 1985. Role of fault bends in the initiation and termination of earthquake rupture, *Science,* **228,** 984–987.

King, G.C.P., 1986. Speculations on the geometry of the initiation and termination processes of earthquake rupture and its relation to morphology and geological structure, *Pure appl. Geophys.,* **124,** 567–585.

King, G.C.P., Oppenheimer, D. & Amelung, F., 1994. Block versus continuum deformation in the Western United States, *Earth planet. Sci. Lett.,* **128,** 55–64.

King, G.C.P., Klinger, Y., Bowman, D. & Tapponnier, P., 2005. Slip-Partitioned Surface Breaks for the Mw 7.8 2001 Kokoxili Earthquake, China, *Bull. seism. Soc. Am.,* **95**(2), 731–738.

Klinger, Y., Xu, X., Tapponnier, P., Woerd, J.V.d., Lasserre, C. & King, G.C.P., 2005. High-resolution satellite imagery mapping of the surface rupture and slip distribution of the $M_W \sim 7.8$, 14 November 2001 Kokoxili Earthquake, Kunlun Fault, Northern Tiber, China, *Bull. seism. Soc. Am.,* **95**(5), 1970–1987.

Kostrov, V., 1974. Seismic moment and energy of earthquakes, and seismic flow of rock, *Phys. Solid Earth,* **1**, 23–44.
Lahr, J.C. & Plafker, G., 1980. Holocene Pacific-North American plate interaction in southern Alaska: implications for the Yakataga seismic gap, *Geology,* **8,** 483–486.
Liu, J., Sieh, K. & Hauksson, E., 2003. A structural interpretation of the aftershock "Cloud" of the 1992 M_W 7.3 Landers Earthquake, *Bull. seism. Soc. Am.,* **93**(3), 1333–1344.
Mandelbrot, B.B., 1982. *The Fractal Geometry of Nature*, W.H. Freeman and Company.
Matmon, A., Schwartz, D.P., Haeussler, P.J., Finkel, R., Lienkaemper, J.J., Stenner, H.D. & Dawson, T.E., 2006. Denali fault slip rates and Holocene-late Pleistocene kinematics of central Alaska, *Geology,* **34**(8), 645–648.
McCaffrey, R., 1992. Oblique Plate Convergence, Slip Vectors, and Forearc Deformation, *J. geophys. Res.,* **97**(B6), 8905–8915.
McCaffrey, R., Zwick, P.C., Bock, Y., Prawirodirdjo, L., Genrich, J.F., Stevens, C.W. & Puntodewo, S.S.O., 2000. Strain partitioning during oblique plate convergence in northern Sumatra: geodetic and seismologic constraints and numerical modeling, *J. geophys. Res.,* **105**(B12), 28 363–28 376.
Mériaux, A.-S., Sieh, K., Finkel, R.C., Rubin, C.M., Taylor, M.H., Meltzner, A.J. & Ryerson, F.J., 2009. Kinematic behavior of southern Alaska constrained by westward decreasing postglacial slip rates on the Denali Fault, Alaska, *J. geophys. Res.,* **114,** 1–19.
Molnar, P., 1979. Earthquake recurrence intervals and Plate Tectonics, *Bull. seism. Soc. Am.,* **69**(1), 115–133.
Molnar, P., 1983. Average regional strain due to slip on numerous faults of different orientations, *J. geophys. Res.,* **88,** 6430–6432.
Nettles, M. & Hjörleifsdóttir, V., 2010. Earthquake source parameters for the January, 2010, Haiti mainshock and aftershock sequence, *Geophys. J. Int.,* **183**(1), 375–380.
Platt, J.P., 1993. Mechanics of Oblique Convergence, *J. geophys. Res.,* **98,** 16 239–16 256.
Ratchkovski, N.A., 2003. Change in stress directions along the central Denali fault, Alaska after the 2002 earthquake sequence, *Geophys. Res. Lett.,* **30**(19), 1–4.
Ratchkovski, N.A. *et al.*, 2003. Aftershock sequence of the Mw 7.9 Denali Fault, Alaska, Earthquake of 3 November 2002 from regional seismic network data, *Seism. Res. Lett.,* **74**(6), 743–752.
Ratchkovski, N.A., Wiemer, S. & Hansen, R.A., 2004. Seismotectonics of the Central Denali Fault, Alaska, and the 2002 Denali Fault earthquake sequence, *Bull. seism. Soc. Am.,* **94**(6B), S156–S174.
Schwartz, D.P., Haeussler, P.J., Seitz, G.G. & Dawson, T.E., 2012. Why the 2002 Denali fault rupture propagated onto the Totschunda fault: implications for fault branching and seismic hazards, *J. geophys. Res.,* **117,** 1–25.
Sieh, K. & Natawidjaja, D., 2000. Neotectonics of the Sumatran fault, Indonesia, *J. geophys. Res.,* **105**(B12), 28 295–28 326.
St. Amand, P., 1957. Geological and Geophysical synthesis of the Tectonics of portions of British Columbia, the Yukon territory and Alaska, *Bull. geol. Soc. Am.,* **68,** 1343–1370.
Stout, J.H. & Chase, C.G., 1980. Plate kinematics of the Denali fault system, *Can. J. Earth Sci.,* **17,** 1527–1537.
Wesson, R.L. & Boyd, O.S., 2007. Stress before and after the 2002 Denali fault earthquake, *Geophys. Res. Lett.,* **34,** L07303, doi:10.1029/2007GL029189.
Wright, T.J., Lu, Z. & Wicks, C., 2003. Source model for the M_w 6.7, 23 October 2002, Nenana Mountain Earthquake (Alaska) from InSAR, *Geophys. Res. Lett.,* **30**(18), 1–4.
Wright, T.J., Lu, Z. & Wicks, C., 2004. Constraining the slip distribution and fault geometry of the Mw 7.9, 3 November 2002, Denali Fault earthquake with interferometric synthetic aperture radar and global positioning system data, *Bull. seism. Soc. Am.,* **94**(6B), S175–S189.
Xu, X., Wen, X., Yu, G., Chen, G., Klinger, Y., Hubbard, J. & Shaw, J., 2009. Coseismic reverse- and oblique-slip surface faulting generated by the 2008 M_W 7.9 Wenchuan earthquake, China, *Geology,* **37**(6), 515–518.
Yu, G., Wesnousky, S.G. & Ekström, G., 1993. Slip partitioning along major convergent plate boundaries, *PAGEOPH,* **140,** 183–210.
Yu, G. *et al.*, 2010. Fault-scarp features and cascading-rupture model for the Mw 7.9 Wenchuan Earthquake, Eastern Tibetan Plateau, China, *Bull. seismol. Soc. Am.,* **100**(5B), 2590–2614.
Zoback, M.D. & Beroza, G.C., 1993. Evidence for near-frictionless faulting in the 1989 (M6.9) Loma Prieta, California, earthquake and its aftershocks, *Geology,* **21,** 181–185.

APPENDIX A: STRAIN ROSETTE REPRESENTATION

The slip vector u associated with an earthquake e is derived from the earthquake focal mechanism (Amelung & King 1997a,b). The geometric moment tensor (King 1978), also called potency (Ben-Menahem & Singh 1981; Ben-Zion 2001; Ben-Zion & Zhu 2002) is then obtained using the following equation (modified from Gilbert 1970),

$$\mathcal{M}_{ij}^{(e)} = \int_A ud\,A(u_i n_j + u_j n_i),$$

where A is the surface of the fault plane that has slipped, n_i the fault normal vector and u_i the unit slip vector. In order to be able to sum the contribution of several earthquakes, the tensor is projected into a global system of geographic coordinates:

$$\mathcal{M}_{\mathrm{NW}} = R\mathcal{M}_{ij}R^T,$$

where R is the rotational matrix.

The strain is then derived following:

$$\varepsilon_{\mathrm{NW}} = (1/2V)\sum_{e=1}^{N}\mathcal{M}_{\mathrm{NW}}^{(e)},$$

where N is the number of earthquakes and V the volume of sampling (modified from Kostrov 1974; Molnar 1979, 1983). Although we prefer to use the geometric moment tensor, it relates to the seismic moment tensor M_{ij} following:

$$M_{ij} = \mu Sd = \mu\mathcal{M}_{ij},$$

with μ the shear modulus, S the surface of the ruptured fault and d the displacement.

It is important to note that the geometric moment and the seismic moment differ in amplitude but not in shape. The absolute value of each component of the strain is less important than the relative value between distinct strain components.

The strain rosette is a representation of the radial component of the strain tensor as a function of the azimuth (Fig. 2). The formula is the following:

$$\varepsilon_{rr} = \varepsilon_{\mathrm{NN}}\cos^2(t) + \varepsilon_{\mathrm{WW}}\sin^2(t) + 2\varepsilon_{\mathrm{NW}}\cos(t)\sin(t),$$

with t the azimuth varying from 0° to 360°.

We use the following colour code:

$\varepsilon_{rr} > 0$: white compressional lobes
$\varepsilon_{rr} < 0$: black extensional lobes.

A.1 Earthquake self-similarity and strain rosette representation

When an earthquake series obeys a power law in amplitude (commonly expressed as b value) and when the associated geometric moment tensors are summed and are consistent with a unique deformation pattern for all spatial scales considered, then such earthquake series is self-similar. This is a fundamental property of fractal systems (Mandelbrot 1982). Amelung & King (1997a,b) checked

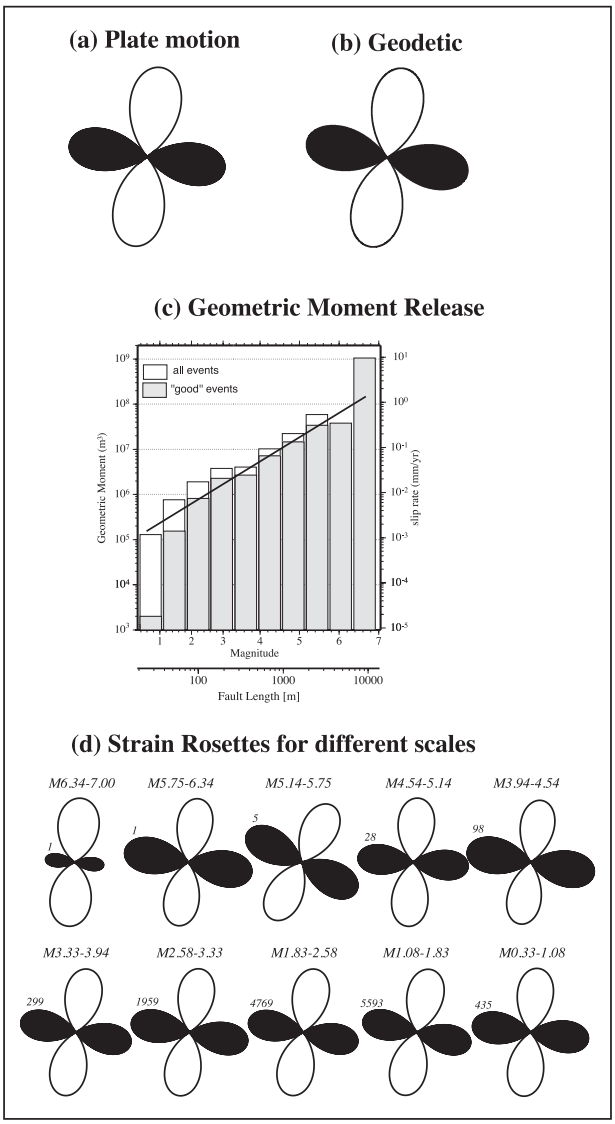

Figure A1. Strain rosettes, shape factors and earthquake scaling relations for the San Francisco Bay area based on Amelung & King (1997a,b). (a) Strain rosette predicted from relative plate motion for the San Francisco Bay area. (b) Strain rosette predicted from geodetic data for the San Francisco Bay area. (c) Scaling relation for 28 years of events for the Bay area. The histogram plots geometric moment against fault length for events between $M0.33$ and M 7.0. Each column considers events in bins with mean fault length differing by a factor two from the adjacent ones. The line indicates the condition where the geometric moment release increases by a factor of 8 for each doubling of average fault length: a simple geometric relation. Small events ($<M1.83$) and large events ($>M5.75$) do not fit this relation. For small events this results from the incompleteness of the catalogue and for large events the time period is too short for the catalogue to be complete. (d) Strain rosettes for the same bins used in c. The number of events used to create the rosettes is indicated. For bins of events less than $M4.55$ the strain rosettes are identical. For the seven events greater $M5.14$ the rosettes differ from those found for smaller events and from the form predicted from plate motion and geodetic data. It is of interest to note that although the largest event releases more moment than all the other events together it is not representative of deformation in the region.

that when the number of earthquakes is large enough this is strictly obeyed (Fig. A1).

Hence, if a given set of earthquakes (such as our Denali series) obeys a power law, one may check that these earthquakes are also consistent with a unique deformation pattern at all spatial scales considered. If this is true, then the earthquake series is self-similar and the expression of the geometric moment $\mathcal{M}_{ij}$ (equivalent to $M.R_{\theta\Phi}$, M being the scalar moment and $R_{\theta\Phi}$ the radial component represented by strain rosettes), can be simplified to only consider the radial term $R_{\theta\Phi}$.

It is widely believed that only the largest earthquakes matter because they represent the largest deformation component and that small events can be ignored. This is not true for the strain rosettes, which should be statistically scale independent. For this reason numerous small events provide a much more reliable determination of $R_{\theta\Phi}$ than a few large events.

APPENDIX B: KINEMATIC APPROACH

B.1 First projection: from the applied plate motion to the slip on the fault plane

The unit plate motion U_{pm} is projected on the fault plane following the direction that is normal to the fault plane. The components of the resulting vector U_{f} (shown by the black arrow in Fig. B1) varies depending on the obliquity and the dip of the fault. The dip slip component U_{df} is given by:

$$U_{\mathrm{df}} = U_{\mathrm{pm}} \cos(dip) \sin(\lambda_{\mathrm{pm}}).$$

The strike-slip component U_{sf} is given by:

$$U_{\mathrm{sf}} = U_{\mathrm{pm}} \cos(\lambda_{\mathrm{pm}}).$$

U_{f} length is:

$$\|U_{\mathrm{f}}\| = \sqrt{\left(U_{\mathrm{sf}}^2 + U_{\mathrm{df}}^2\right)}$$

The slip rake, that is, the angle of the slip vector from the x-axis varies with the fault obliquity and the fault dip as follows (Fig. B2),

$$\tan(rake) = U_{\mathrm{df}}/U_{\mathrm{sf}} = [U_{\mathrm{pm}} \cos(dip) \sin(\lambda_{\mathrm{pm}})]/[U_{\mathrm{pm}} \cos(\lambda_{\mathrm{pm}})]$$
$$= \cos(dip) \tan(\lambda_{\mathrm{pm}}).$$

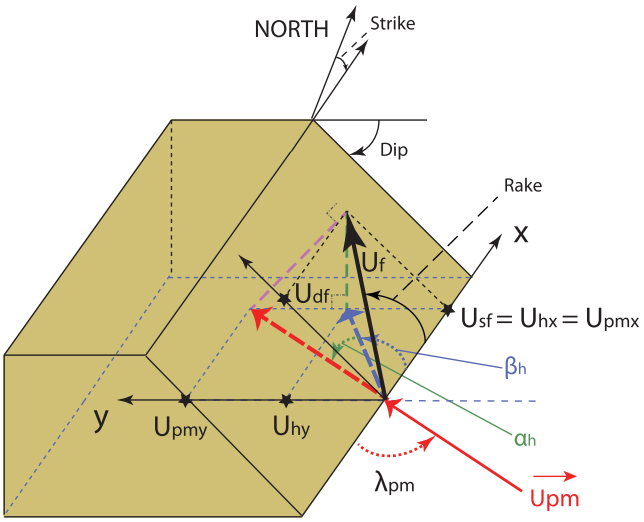

Figure B1. The plate-motion (red unit vector) is projected onto the fault (black arrow) following the purple dashed line normal to the fault. The slip on the fault (black arrow) is projected onto the horizontal plane (blue arrow) following the green dashed line normal to the horizontal plane.

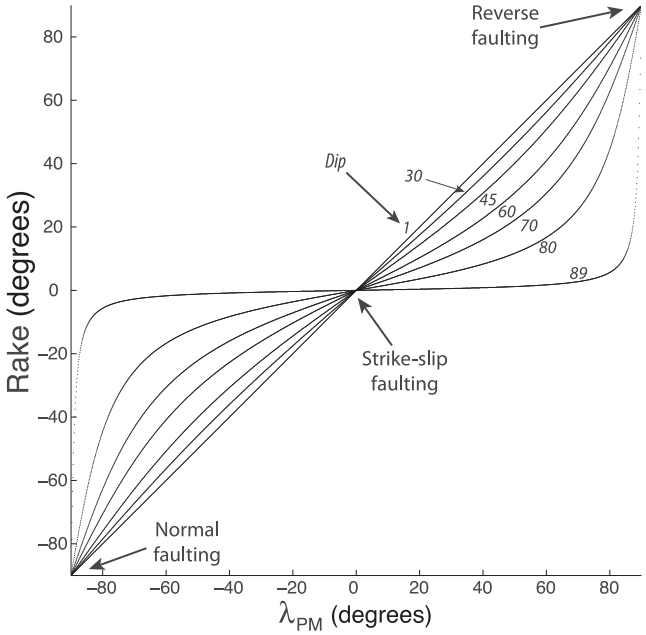

Figure B2. Variation of the rake of the slip taken up on the fault as a function of the fault obliquity and dip.

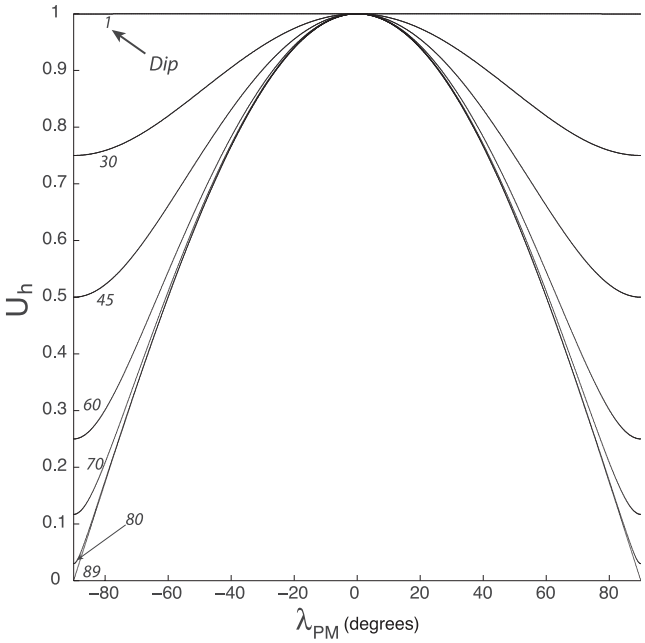

Figure B3. Variation of the amplitude of the horizontal slip (U_h) taken up by sliding on the fault as a function of the fault obliquity and the fault dip.

B.2 Second projection: from the slip on the fault plane to the horizontal displacement that is accommodated

U_f is projected onto the horizontal plane following the direction that is normal to the horizontal plane. The resulting vector U_h (shown by the blue arrow in Fig. B1) corresponds to the horizontal displacement actually accommodated by sliding on the fault. The x and y components vary with the fault obliquity and the fault dip as follows:

$$U_{hy} = U_{df}\cos(dip) = U_{pm}\cos^2(dip)\sin(\lambda_{pm}),$$
$$U_{hx} = U_{sf} = U_{pm}\cos(\lambda_{pm}).$$

U_h length is then (Fig. B3):

$$\|U_h\| = \sqrt{\left(U_{hy}^2 + U_{hx}^2\right)},$$

while the angle β_h between U_h and the x-axis is obtain from:

$$\tan(\beta_h) = U_{hy}/U_{hx} = \cos^2(dip)\tan(\lambda_{pm}).$$

The angle between the initial horizontal plate motion and the horizontal motion, α_h, accommodated by the fault is eventually calculated as follows (Fig. B4):

$$\alpha_h = \lambda_{pm} - \beta_h = \lambda_{pm} - \tan^{-1}[\cos^2(dip)\tan(\lambda_{pm})].$$

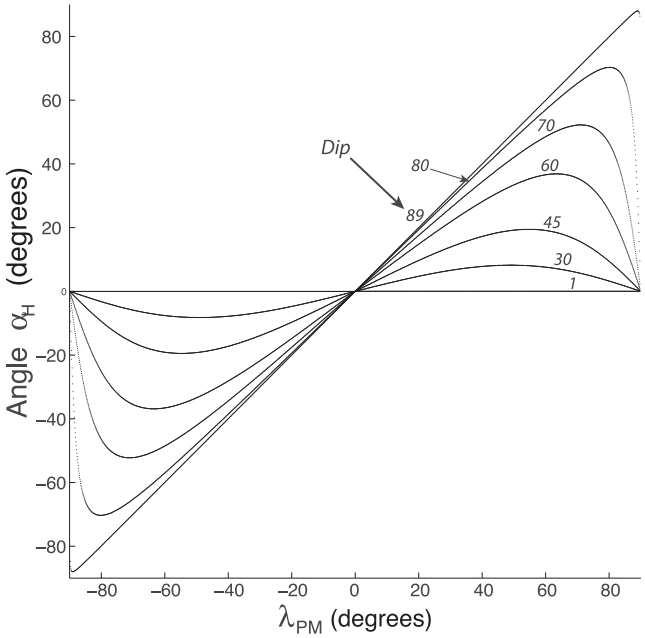

Figure B4. Variation of the angle between the horizontal slip taken up by sliding on the fault (U_h) and the applied plate motion (U_{pm}) as a function of the fault obliquity and dip.

B.3 Third projection: the coefficient of accommodation

The displacement accommodated horizontally by sliding on the fault plane is different from the applied plate motion in amplitude as well as in orientation. By projecting the first vector onto the second one, we can calculate a coefficient of accommodation Ca that quantifies the ability of the pre-established fault to release the applied plate motion. The coefficient of accommodation is given by:

$$Ca = ||U_h||\cos(\alpha_h)/||U_{pm}||.$$

APPENDIX C: STUDY OF EARTHQUAKE CATALOGUE

In the main body of the paper, we consider separately the main shock, the aftershocks and the background seismicity. Here are given more details about how we split data into these three datasets (Figs C1 and C2).

We have also calculated the earthquake occurrence, distinguishing between the 2002–2004 time periods and the 2005–2011 time periods and for the three areas of interest described in the paper.

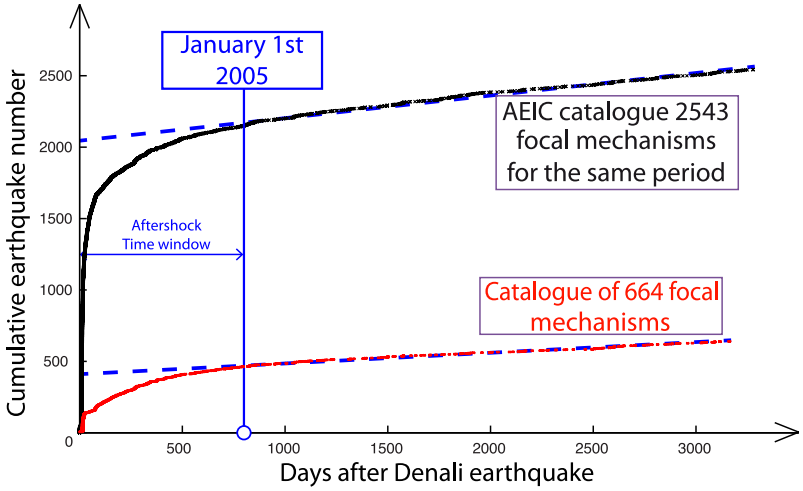

Figure C1. Cumulative earthquake number as a function of time after Denali earthquake. Two data sets are plotted, our catalogue of 664 focal mechanisms and the 2543 earthquakes registered during the same period by the AEIC (no focal mechanisms for this dataset). We decided to end the aftershock sequence on 2005 January 1 (blue line), when the rate of seismicity becomes constant.

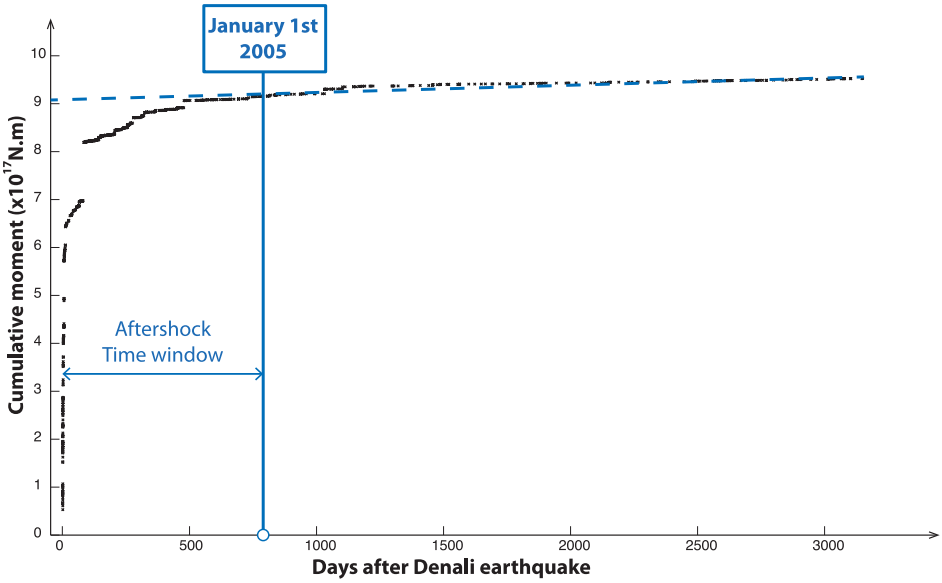

Figure C2. Cumulative moment released by earthquakes as a function of time after Denali earthquake. The blue line indicates the time at which we split the catalogue between the aftershocks and the background seismicity. After the 2005 January 1, the rate of earthquakes seems constant.

It is important to note that many earthquakes occur outside of the zones we study.

(1) 1987–2002 ~ 5780 d
  (i) West: 23 earthquakes ~ 0.004 eq d^{-1}
  (ii) Centre: 30 earthquakes ~ 0.005 eq d^{-1}
  (iii) East: 7 earthquakes ~ 0.001 eq d^{-1}
(2) 2002–2004 ~ 790 d
  (i) West: 207 earthquakes ~ 0.26 eq d^{-1}
  (ii) Centre: 160 earthquakes ~ 0.2 eq d^{-1}
  (iii) East: 74 earthquakes ~ 0.1 eq d^{-1}
(3) 2005–2011 ~ 2555 days
  (i) West: 62 earthquakes ~ 0.024 eq d^{-1}
  (ii) Centre: 38 earthquakes ~ 0.015 eq d^{-1}
  (iii) East: 32 earthquakes ~ 0.013 eq d^{-1}

The seismicity between 2005 and 2011 is 10 times higher than between 1987 and 2002, but it remains 10 times lower than the one between 2002 and 2004. It is furthermore likely that the number of earthquakes occurring between 1987 and 2002 is a minimum number because the deployment of temporary seismic stations after the Denali earthquake has improved the ability to record small earthquakes after 2002. We then tend to interpret the 2005–2011 period as the start of the interseismic period with a quite high seismicity rate (induced by the occurrence of the 2002 sequence) with respect to the period prior to the earthquake. Putting together or not these two periods does not change the resulting rosettes substantially (Fig. 8a versus 9a), but making the distinction allows us to make hypothesis on the pattern of deformation at distinct periods of the seismic cycle.